

# Traffic Image Dehazing Using Sky Segmentation and Color Space Conversion\*

FAN GUO, JUN-FENG QIU, JIN TANG<sup>†</sup> AND WEI-QING LI

*School of Automation  
Central South University  
Changsha, 410083 P.R. China  
E-mail: tjin@csu.edu.cn*

In order to restore degraded traffic images in haze and dark environment, we present an efficient traffic image haze removal method using sky segmentation and color space conversion. The dark channel++ and contrast energy++ features are proposed for the fast sky segmentation step. The atmospheric light is estimated based on the haze density in different region, and the dehazing procedure is executed in HSI color space. Besides, this method takes advantage of the contrast limited adaptive histogram equalization (CLAHE) and guided image filtering to ensure a visual pleasing result. The experimental results for both synthetic and natural hazy images demonstrate that our algorithm performs comparable or even better results than the state-of-the-art methods in terms of various measurement indexes, such as the MSE, SSIM, mean gradient change rate, *etc.* Two traffic applications, such as road-marking extraction and vehicle detection, are presented to verify the effectiveness of the proposed algorithm.

**Keywords:** traffic scene, image dehazing, sky segmentation, color space conversion, traffic applications

## 1. INTRODUCTION

Haze is a common natural phenomenon which is caused by the turbid medium (*e.g.*, water droplets, particles, *etc.*) in the atmosphere. As we all know, haze will do great harm to human's manufacture and life if it occurs in urban scene. On the one hand, haze drastically reduces visibility which will cause some serious accidents. On the other hand, the pollutants in the air are a serious threat to human health. And the former is particularly serious. To solve the first problem, many scientists do research on the inherent reason of the fog image formation. The mathematical model established by McCartney [1] is the most famous. Based on the atmospheric scattering model, together with the increase of observation distance, the intrinsic luminance of the observed object decays according to exponential distribution, and the luminance of the atmospheric light increases gradually. Hence, the image quality captured by sensors decreases as the distance increases.

In the domain of transportation, the appearance of haze will bring bad effect for self-driving system, driving assistance system [2], traffic surveillance system [3], *etc.* As we all know, the image sensors play an important role in traffic scenes and the surveillance videos can help the traffic police judge the legal liability in traffic accidents. However, in haze weather the number of traffic accidents increases greatly, but the traffic surveillance system cannot get clear accident pictures which bring bad effects for traffic accidents determination. Besides, the traffic violation detection system is unable to work so that the

---

Received February 21, 2020; revised August 6, 2020; accepted August 31, 2020.

Communicated by Wen-Liang Hwang.

\* This research was funded by the National Natural Science Foundation of China (Grant No. 61502537), and the Hunan Provincial Natural Science Foundation of China (Grant No. 2018JJ3681).

road safety is more severe.

Since we suffer from haze in traffic scene, so many researchers proposed various approaches to perform haze removal. These methods can be divided into two categories: iconology-based algorithms and physics-based algorithms. The first kind is mainly based on image enhancement like histogram equalization which just improve the image contrast. The second kind primarily based on the atmospheric scattering model which handle the problem with mathematical method, but it may cause other problems such as color distortion, halo artifacts, missing details. Therefore, this paper proposed a novel haze removal method using color space conversion and sky segmentation. Experimental results show that the proposed method can avoid color distortion and halo artifacts after dehazing and obtain more natural haze-free images. Besides, the traffic image sensors often work in dark condition, so we increase brightness and restore detail information by image enhancement. The proposed method takes full advantages of the iconology-based and physics-based methods, and thus it can obtain visual pleasing results and even work well in dark environment.

The rest of this paper is organized as follows. In Section 2, the related works about the single image dehazing algorithms and their application in traffic field are reviewed. Section 3 introduces the proposed haze removal algorithm for traffic images. The experimental results are given in Section 4. Finally, Section 5 concludes this paper.

## 2. RELATED WORKS

The inherent reason of the formation of fog image can be described using the atmospheric scattering model which is established by McCartney [1]. Based on the mathematical model, other researchers make some improvements [4-7] so the complex model can be simplified as follows:

$$I(i, j, k) = J(i, j, k)t(i, j, k) + A(1-t(i, j, k)) \quad (1)$$

where  $i$  and  $j$  are the row index and the column index of the pixel in the single-channel image, and  $k$  is the index of channel.  $I$  is the observed hazy image which represents the intensity can be received by image sensors.  $J$  is the restored haze-free image which represents the intrinsic luminance of the observed object.  $A$  is the atmospheric light value which is fixed in this model. And  $t$  is the transmission map which is related to the depth map. We can easily find that haze removal is an ill-posed problem according to Eq. (1). Hence, many researchers try to propose various constraints or priors to obtain the haze-free image.

The majority of early dehazing approaches rely on depth information directly or multiple images of the observed scene. From the atmospheric scattering model, we can find that there is a functional relation between transmission map and depth map. Hence, Kopf *et al.*, propose an approach for haze removal which is just suitable for the scene known depth information or other equipment like calibrated radar to obtain additional information. Schechner *et al.*, [8] perform haze removal by using multiple images acquired from different polarization angles which is based on the observation that the light scattered by the turbid medium is partially polarized. Park *et al.*, [9] propose a method to calculate the depth map by using stereo images. Chen *et al.*, [10] and Narasimhan *et al.*, [11] find that two images taken in different weather conditions can be used for depth information estimation. These methods all need additional constraints which cannot be estimated by the

single image directly so the practical application is difficult.

Recently, many researchers propose various algorithms to solve the issues discussed above and make significant progress in single image haze removal. Through large-scale statistical analysis, Tan [12] assumes that the contrast ratios of haze-free images are higher than that in hazy images. Therefore, he restores the hazy image by maximizing the local contrast and the most haze in the image is removed. However, this method is essentially based on image enhancement, so it brings some bad effects like over-saturation and color distortion and its visual effect is sometimes displeasing. Under the assumption that the transmission shading and surface shading have no correlation in local regions, Fattal [13] deduces the scene transmission by estimating the albedo of the scene. The results obtained by this method are impressive in most cases, but it is time-consuming and the poor performance in dense-hazy images cannot be tolerated. He *et al.*, [14] propose a novel image prior – dark channel prior based on a kind of statistics of the haze-free natural images. Using this prior and the atmospheric scattering model, high quality haze-free images can be obtained. But the restored results are bad once the prior is invalid. Besides, the process of soft matting is time-consuming which limits its application. Tarel *et al.*, [15] make some improvements on He's method and they use median of median filter replace soft matting which significantly reduce the complexity of the algorithm. The speed of the method is competitive until now, but color distortion and image noise problems need some optimization. Meng *et al.*, [16] make some explore on the inherent boundary constraint on the transmission function and then propose an efficient regularization method which can provide pleasing restored images. Although it avoids too dark haze-free results compared with He's, the halo artifacts are more serious. Berman *et al.*, [17] settle the dehazing problem from another perspective and they propose a new non-local prior. This method bases on the observation that a haze-free image color is well approximated by a few hundred distinct colors that form tight clusters in RGB space and the color clusters become haze-lines in corresponding hazy image. It performs well on various images and its efficiency is high. However, the performance maybe bad in images with heterogeneous haze since the dense haze regions are judged as sky. In [18], Zhu *et al.*, present an effective prior - color attenuation prior and create a linear model for estimating the depth information of the hazy image. To obtain the parameters of the model, they use a supervised learning method. Its dehazing results seem more natural, but the haze removal effect seems worse than other methods. Dong *et al.*, [19] modify the imaging model by introducing an additive Gaussian white noise and establish a unified probability framework. Then they estimate unknown variables iteratively until convergence by imposing some reasonable statistical priors on them. Experimental results show that the method works well in the transition zone. To avoid the halo artifacts in dehazing images, Li *et al.*, [20] propose a new approach combining with dark channel prior and sky segmentation to perform haze removal. The visibility of the restored images improves significantly. Wang *et al.*, [21] find some images with an uneven haze density, so they divide a hazy image into several regions through a superpixel segmentation algorithm and then estimate the local atmospheric light in each image region. Qu *et al.*, [22] present a novel haze removal method which is based on a local consistent Markov random field framework. Their approach has the combined advantages of detailed recovery and color preservation, but the time complexity is too high, and 42 seconds are needed for processing an image with a size of 640×480. Lately, as convolutional neural networks (CNNs) have witnessed prevailing success in computer vi-

sion tasks, they have been introduced to image dehazing as well. Cai *et al.*, [23] introduced an end to end system called DehazeNet for estimation of the transmission matrix. Based on reformulated atmospheric model as a substitute of estimating transmission matrix and atmospheric light, Li *et al.*, [24] propose a light-weight AOD-Net model.

The above researchers try to propose a universal haze removal algorithm which can be applied to different scenes. However, different scenes like UAV images and traffic images have various characteristics so that it is necessary to optimize the algorithms for different scenes. Yoon *et al.*, [25] present a spatially-adaptive haze removal method that merges color histograms with consideration of the wavelength-dependent atmospheric turbidity. This algorithm can mitigate the color distortion problem and work well without additional optical equipment. For traffic scenes, Bhoir *et al.*, [26] propose a dehazing method using white balance, saliency feature extraction map, foreground region preservation map and contrast enhancement for remote surveillance system. Yan *et al.*, [27] present a new approach for recognizing the speed limit sign in hazy weather. In the haze removal process, they add a parameter to the transmission of the dehazing equation to make the restored image more natural and have no halo artifacts and color distortions in sky areas. To reduce computing time, Dong *et al.*, [28] propose a traffic video dehazing approach based on the adaptive dark channel prior and spatial-temporal correlations. They also estimate the degree of haze in each image so that the adaptability of the algorithm is strong. Their method is quite efficient and can restore the video with a size of 720×480 at about 57 frames per second. However, some shortcomings such as missing details and bad performance in dark environment still exist. Optimization for specific problems can improve the performance of the dehazing system.

Thus, we can see that most existing haze removal algorithms mainly focus on a general platform or just consider image enhancement or physical model. The focus of our work is traffic scene haze removal and we take full advantage of iconological method and physical method to obtain better dehazing results. The main novelty of our work is that we proposed an adaptive dehazing algorithm for traffic scenes using sky segmentation, local atmospheric light estimation, color space conversion and image enhancement. Since our approach is physically valid, it can provide good dehazing performance even in dark traffic scenes and can well retain the fidelity of the colors and detail information as well.

### 3. PROPOSED METHOD

For the proposed method, we assume that the sky region is an essential part in traffic scenes based on a large-scale of statistics and then propose our haze removal algorithm. First, we perform sky segmentation in hazy images using several haze-relevant features which imply the scene depth. Then we divide a hazy image into several regions according to its haze density. Next, the local atmospheric light is estimated and the transmission map is deduced in the HSI color space for adaptive haze removal. Finally, image enhancement as an image post-processing step is executed for the color fidelity and detail information.

#### 3.1 Sky Segmentation in Hazy Image

The majority of the existing sky segmentation methods try to get an adaptive classifier which can be used for sky segmentation in various scenes. For this purpose, many research-

ers try to extract many quantitative unique characteristics for sky regions, and then rough sky segmentation results can be obtained using a suitable classifier. For reducing misclassification, they conduct a post-processing step to increase the segmentation accuracy.

Although the results of refined sky segmentation are satisfying using the above method, the executing time is long. The time consumption of rough sky segmentation is low, but the corresponding results are unsatisfying. Hence, we propose our sky segmentation approach for high adaptability and efficiency and its schematic diagram is show in Fig. 1. First, we extract two major characteristics from a hazy image as inputs for *k*-means clustering algorithm. Then, we obtain the rough sky segmentation result and further extract the most likely regions of the sky and non-sky from the preliminary result. Next, we calculate other important characteristics (*e.g.* color features, gradient features, position features, *etc.*) from the hazy image and use the training label obtained in the previous step to train the SVM classifier. Finally, we can get the refined sky segmentation results which is accurate enough for further processing.

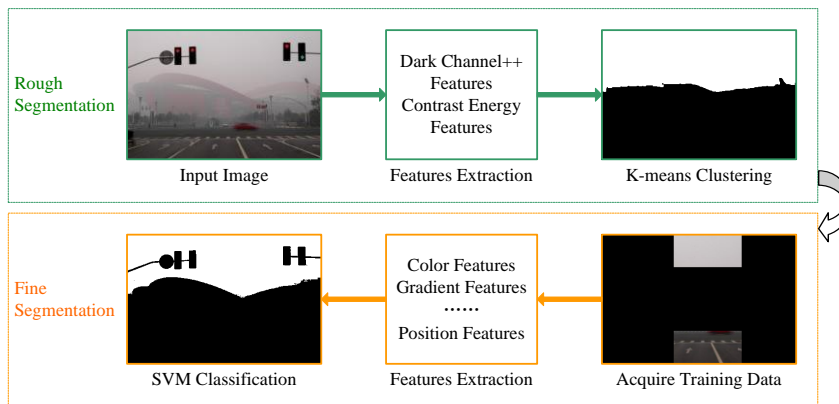


Fig. 1. Framework of the proposed sky segmentation approach.

(A) Features Extraction

For the sky segmentation, the better features we obtain, the better performance of sky segmentation. Thus, we try various characteristics for the traffic scenes. These characteristics used here are called dark channel++ and contrast energy++ are introduced as follows:

The dark channel is valid in non-sky regions which approximates the haze denseness. In sky regions, the intensities of pixels are high in all dark channel. Hence, the dark channel map can be used as a good feature for sky segmentation in natural scenes. However, for traffic scene as shown in Fig. 2 (b), the dark channel feature is invalid on some regions, such as white lane and gray road. These regions will be partially clustered as sky region.

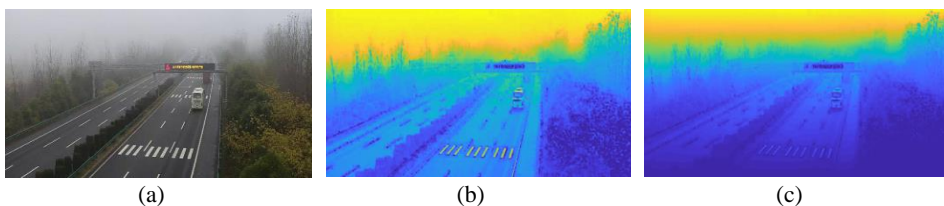


Fig. 2. Dark channel++ feature extraction; (a) Input hazy image; (b) Dark channel; (c) Dark channel++.

Considering the majority of traffic image sensors are vertical to the ground, the smaller row number in the image, the greater distance between the object and the image sensors. Based on the observation, we introduce the row number as the additional information to upgrade the dark channel, as shown in Eq. (2).

$$F_{DC++} = \frac{M}{i} \min_{c \in \{r, g, b\}} I^c(i, j) \quad (2)$$

where  $i$  and  $j$  are the row index and the column index of the pixel, and  $M$  is the sum of the rows.  $I$  is the input hazy image consisting of  $R, G, B$  channels. We also calculate the dark channel++ map which is shown in Fig. 2 (c). The color of sky regions become warmer and the color of foreground objects is colder than before. Besides, the regions in the foreground of dark channel++ which is not applicable for the typical dark channel show the satisfying results.

To predict the perceived local contrast on natural images, Choi *et al.*, [29] employed contrast energy which contains color information and gradient information. The contrast energy map of Fig. 3 (a) is shown in Fig. 3 (b), we can find that the values in sky region and non-sky region are diverse. However, the difference between two regions is unapparent and the boundary is fuzzy in traffic scenes.

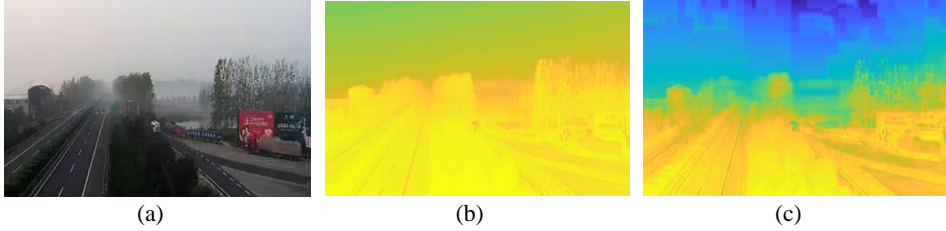


Fig. 3. Contrast energy++ feature extraction; (a) Input hazy image; (b) Contrast energy; (c) Contrast energy++.

To make up for the deficiency of this feature, we add row number information and luminance information to the calculation process of contrast energy++. The process can be written as Eqs. (3)-(5):

$$F_{CE++} = \frac{\alpha \cdot Z(i, j)}{Z(i, j) + \alpha \cdot k} - \tau \quad (3)$$

$$Z(i, j) = \sqrt{(I(i, j) \otimes g_h)^2 + (I(i, j) \otimes g_v)^2} \quad (4)$$

$$I(i, j) = \frac{[0.5(R + G) - B] + i}{(R + G + B) / 3} \quad (5)$$

where  $i$  and  $j$  are the row index and the column index of the pixel and  $R, G, B$  are the three channels of the input hazy image. The symbol  $\otimes$  indicates convolution, and  $g_h$  and  $g_v$  are the horizontal and vertical second-order derivatives of the Gaussian function respectively.

$\alpha$  is the maximum value of  $Z(i, j)$ ,  $k$  is a contrast gain fixed at 0.1, and  $\tau$  is the noise threshold fixed at 0.2287. The obtained contrast energy++ map using our method shows a better visual appearance, since the difference between two regions increases and the boundary seems clearer.

### (B) Segmentation Method

Inspired by the existing sky segmentation methods, we propose our segmentation method using the rough to fine scheme. The main steps of our approach include k-means clustering, training data extraction and SVM classification which are introduced in details as follows.

In the feature extraction stage, we obtain two complementary features which can differentiate sky regions and non-sky regions with high robustness. Hence, we can utilize them as inputs for unsupervised learning algorithm –  $k$ -means clustering to get the preliminary segmentation results, and the detailed steps are as follows:

- Step 1:** Transform the two-dimension dark channel++ and contrast energy++ matrices to column vectors and perform normalization.
- Step 2:** Take the two column vectors as inputs, set the number of clusters to two and perform clustering to get the cluster indices and the cluster centroid locations.
- Step 3:** Determine sky regions and non-sky regions according to the cluster centroid locations.
- Step 4:** Transform the cluster indices vector to a two-dimension binary image with the same size as the hazy image.

The rough sky segmentation results are shown in Fig. 4 (b). Although the boundary between two regions are not accurate, most regions of the result are correct. Thus, we can extract the most likely regions of the sky and non-sky from the above result for further processing.



(a) Input hazy image.

(b) Rough segmentation results.

(c) Fine segmentation results.

Fig. 4. Sky segmentation results.

Based on a large-scale of statistics, we give two assumptions regarding the sky regions in binary images: (i) the proportion of sky regions must more than 0.1; and (ii) the sky regions must be partly or totally at the top of the images. Using the assumptions, we propose our method to extract the most likely sky regions which is introduced in details in Algorithm 1, and the non-sky regions can be extracted through a similar process.

---

**Algorithm 1: Sky Region Training Data Extraction**


---

Input: the rough segmentation map  $B_0$ , the number of rows  $M$ , and the number of columns  $N$

Output: sky region range  $[0, p_{\min}; M/10, p_{\max}]$

Auxiliary function:

function for returning the first index of zero in a vector:  $out = \text{find}_0(in)$

function for returning the indexes of the longest num subsequence in a vector:  $[first, last] = \text{maxsubsequence}(in, num)$

Begin

1:  $s[N] = \{0\}$ ;

2: for index from 1 to  $N$  do

3:  $s[j] = \text{find}_0(B_0(:, j))$ ;

4: end for

5:  $p_{\min} = 0; p_{\max} = 0$ ;

6: for index from 1 to  $N$  do

7:  $s[j] \geq M/10 ? M/10 : 0$ ;

8: end for

9:  $[p_{\min}, p_{\max}] = \text{maxsubsequence}(s, M/10)$ ;

End

---

Now, we can obtain the training data of sky regions and non-sky regions. To improve the applicability of the SVM classifier, we need more good features like color saturation, hue disparity, Canny edge, color gradient. All above features are extracted from the hazy image using the method [30]. Then we combine the dark channel++ feature, the contrast energy++ feature and the above four features as inputs for supervised learning algorithm - SVM to get the refined segmentation results, as shown in Fig. 4 (c).

The classification process is described as follows. First, we transform the feature matrices in ROI regions to column vectors and train the SVM classifier. Then, the feature matrices in whole hazy image are transformed to column vectors and the label of pixels can be obtained. Finally, we transform the label vector to a binary image with the same size as the hazy image. Experimental results show that the proposed sky segmentation algorithm is simple but effective in both precision and efficiency, and most traffic road scenes generally have sky region. Thus, it can be used in traffic dehazing applications.

### 3.2 Atmospheric Light Estimation

The distribution of haze density is inconsistent across the entire image. However, the majority of existing methods neglect the haze density and fix the atmospheric light value for model simplification which cause over-enhancement and the remaining haze in local regions. Besides, the atmospheric light is not always uniform in an image so that the re-

stored image is prone to suffer from halo artifacts and uneven brightness. Hence, a novel atmospheric light estimation method is proposed, which consists of four parts, as shown in Fig. 5.

First, we perform region division based on haze density via a simple but effective method –  $k$ -means clustering, and the input image is divided to three parts including sky region (dense haze region), medium haze region and thin haze region. Then, we find the brightest region of the image using a hierarchical searching method based on quad-tree subdivision, and the mean value of the region can be regarded as the atmospheric light in dense haze region. Next, a statistical method is used to calculate the atmospheric light in thin haze region. Finally, we conduct a series of smooth processing to avoid sudden change of the atmospheric light values.

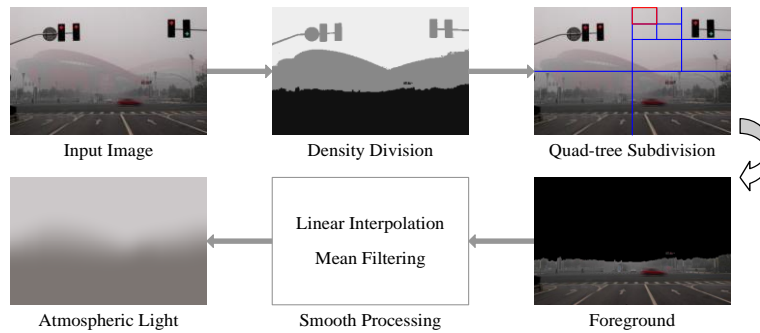


Fig. 5. Illustration of the proposed atmospheric light estimation approach.

#### (A) Haze Density Region Division

In Section 3.1, we realize sky segmentation in hazy image so that we can easily extract non-sky regions from images now. Besides, the dark channel++ of a hazy image approximates the haze denseness well and is not affected by white lane or gray road. Hence, the dark channel++ feature can be used as a vector for  $k$ -means clustering that realizes haze density division in non-sky regions. However, the results of  $k$ -means clustering in our experiment show that the regions with similar haze density is discontinuous that may cause some noise in local regions. To avoid this problem, we introduce the position feature which has relationship with the distance between the objects and the image sensor. The realization process can be described as:

- Step 1:** Calculate the dark channel++ matrix and set the element values in sky region to minus one.
- Step 2:** Calculate and normalize the position matrix that is each element of every row equals the row number divided by the number of rows and note that the element value in sky region are set to minus one.
- Step 3:** Transform the two-dimension dark channel++ and position matrices to column vectors.
- Step 4:** Take the two column vectors as inputs, set the number of clusters to three and perform clustering to get the cluster indices and the cluster centroid locations.

**Step 5:** Determine sky region, medium haze region and thin haze region according to the cluster centroid locations.

**Step 6:** Transform the cluster indices vector to a two-dimension gray image with the same size as the hazy image.

#### (B) Atmospheric Light in Distant Regions

In traffic scenes, the sky regions are always essential parts of images. Besides, the sky region is always the brightest of the whole image based on statistical analysis. Thus, we make some improvements on traditional quad-tree decomposition algorithm that can be used in images with random sizes. To extract the atmospheric light in distant region, the following steps are conducted.

First, we set the stopping condition that is the difference value between maximum value and minimum value of the mean values of the corresponding four region is less than 0.1, and input the hazy image. Then, the hazy image is decomposed to four approximately equal regions and the mean value of pixels in each sub-block are calculated that is the score of each sub-region. Next, the sub-region with the highest score are decomposed until the stopping condition is satisfied. Finally, the brightest region of the image can be obtained and the atmospheric light in distant region is obtained.

#### (C) Atmospheric Light in Near Regions

In Section 3.2(A), the gray image which represents the haze density in different regions is obtained. Here, we can use it to set the values of pixels in other regions to zero and extract the thin haze region which can be used as the input. The main route to realize atmospheric light estimation by statistical method is extracting the brightest pixels in top 1 percent, and then calculate the mean value of these pixels. More details about atmospheric light estimation in near regions are shown in Algorithm 2.

---

#### **Algorithm 2:** Atmospheric Light Estimation in Near Regions

---

Input: the thin haze region  $I_f$ , and the cumulative probability  $p$

Output: atmospheric light [ $whiteR$ ,  $whiteG$ ,  $whiteB$ ]

Auxiliary function:

function for converting the true color image  $RGB$  to the grayscale image  $I$ :  $I = \text{rgb2gray}(RGB)$

function for returning quantiles of the elements in vector  $X$  for the cumulative probability  $p$  in the interval  $[0, 1]$ :  $Y = \text{quantile}(X, p)$

function for returning the row and column indexes of the elements satisfying conditions in array  $X$ :  $[\text{row}, \text{col}] = \text{find}(X, \text{conditions})$

function for returning the linear indices  $ind$  corresponding to the row, column and dimension subscripts in  $row$ ,  $col$  and  $dim$  for a matrix of size  $sz$ :  $ind = \text{sub2ind}(sz, row, col, dim)$

function for returning a row vector whose elements are the lengths of the corresponding dimensions of  $A$ :  $sz = \text{size}(A)$

function for returning an array of ones where the size vector,  $sz$ , defines  $\text{size}(A)$ :  $X = \text{ones}(sz)$

function for returning the mean along dimension  $dim$ :  $M = \text{mean}(A, dim)$

---

---

Begin

```

1:  $I_{fg} = \text{rgb2gray}(I_f)$ ;
2:  $i_{val} = \text{quantile}(I_{fg}(:, :), p)$ ;
3:  $[r_{ind}, c_{ind}] = \text{find}(I_{fg} >= i_{val})$ ;
4:  $sel(:, 1) = I_f(\text{sub2ind}(\text{size}(I_f), r_{ind}, c_{ind}, \text{ones}(\text{size}(r_{ind}))))$ ;
5:  $sel(:, 2) = I_f(\text{sub2ind}(\text{size}(I_f), r_{ind}, c_{ind}, 2 * \text{ones}(\text{size}(r_{ind}))))$ ;
6:  $sel(:, 3) = I_f(\text{sub2ind}(\text{size}(I_f), r_{ind}, c_{ind}, 3 * \text{ones}(\text{size}(r_{ind}))))$ ;
7:  $[whiteR, whiteG, whiteB] = \text{mean}(sel, 1)$ ;

```

End

---

#### (D) Smooth Processing

Although we obtain the atmospheric light values in dense haze region and thin haze region, we cannot use it directly due to the sudden change of atmospheric light values in neighboring regions. To avoid this problem, we take the medium haze region as a transition region and perform interpolation in vertical direction of the atmospheric light map. This operation is just effective in images always contain sky regions in the first few rows. As shown in Fig. 6 (a), the sky region just takes the left upper part of the image, so the sudden change in horizontal direction is serious. For further smooth processing, we perform mean filtering on the preliminary atmospheric light map and the final result is satisfying, as shown in Fig. 6 (c).



(a) Input hazy image.

(b) Interpolation result.

(c) Mean filtering result.

Fig. 6. Smooth processing result.

### 3.3 Physics-based Haze Removal in HSI Color Space

Single image dehazing is a challenging problem in the computer vision field, and many researchers try to solve the problem in RGB color space. Thus, various novel priors (*e.g.*, dark channel prior, non-local prior, color attenuation prior, *etc.*) are proposed. However, many other problems (*e.g.*, color distortion, halo artifacts, missing details, *etc.*) are produced to the restored images that affect the image quality. Considering different priors possess different advantages, we try to take advantages of various effective priors and propose a haze removal algorithm based on HSI color space. The proposed method consists of four parts.

First, we perform color space transformation on the hazy image and extract the H, S, and I matrices, respectively. Then, the I channel can be restored and the relationship between I and S matrices are deduced, and the restored S channel can be obtained. Finally, we keep the H channel fixed and get the preliminary dehazing results.

#### (A) Color Space Transformation

As show in Eq. (6), the transformation formulas are not complex, and the dark channel

prior and non-local prior can be easily combined in HSI color space. The process can be written as:

$$\begin{cases} H = \begin{cases} \theta & G \geq B \\ 2\pi - \theta & G < B \end{cases} \\ S = 1 - \frac{3 \min(R, G, B)}{R + G + B} \\ I = \frac{R + G + B}{3} \end{cases} \quad (6)$$

where  $\theta = \arccos \left( \frac{(R-G) + (R-B)}{2\sqrt{(R-G)^2 + (R-B)(G-B)}} \right)$ .

In [14], He *et al.*, propose a dark channel prior based on a kind of statistics of the haze-free natural images. The prior can be described using Eq. (7) that means at least one-color channel having very low intensity at some pixels in most of the non-sky regions.

$$J^{dark}(x) = \min_{c \in \{r, g, b\}} (\min_{y \in \Omega(x)} (J^c(y))) \quad (7)$$

where  $J^{dark}$  is the dark channel of  $J$  tending to be zero,  $J^c$  is a color channel of  $J$  and  $\Omega(x)$  is a local region that is centred at  $x$ . In HSI color space, we can perform the max operation on  $S$  channel and insert Eq. (7) into the equation, thus the similar prior can be obtained.

$$\max_{y \in \Omega(x)} (S) = 1 - \frac{3}{R + G + B} J^{dark}(x) \quad (8)$$

where  $3/(R+G+B)$  is always positive, and  $J^{dark}(x)$  tends to be zero, so the Eq. (8) can be simplified to Eq. (9).

$$\max_{y \in \Omega(x)} (S) = 1 \quad \max_{y \in \Omega(x)} (S) = 1 \quad (9)$$

Hence, the dark channel prior has an equivalent definition in HSI color space that can be applied in different ways. In [17], Berman *et al.*, observe that colors of a haze-free image are well approximated by a few hundred distinct colors forming tight clusters in RGB space, and the color clusters become haze-lines in corresponding hazy image. To show the observation clearly, we depict the haze-lines in RGB and HSI color space respectively, as shown in Figs. 7 (a) and (b). In most haze conditions, the airlight is tend to pure white, so the haze-lines can be assumed to pass through the fixed point. Furthermore, it is obvious that the hue value is invariant by projecting haze-lines on to the HS plane, as shown in Fig. 7 (c). Hence, we take this strategy to keep the color fidelity.

#### (B) Transmission Map of I Channel

In essence, the I channel image is a gray image, satisfying the atmospheric scattering model which is shown in Eq. (1), and the I value has linear relationship with R, G and B values. Hence, Eq. (10) can be easily deduced.

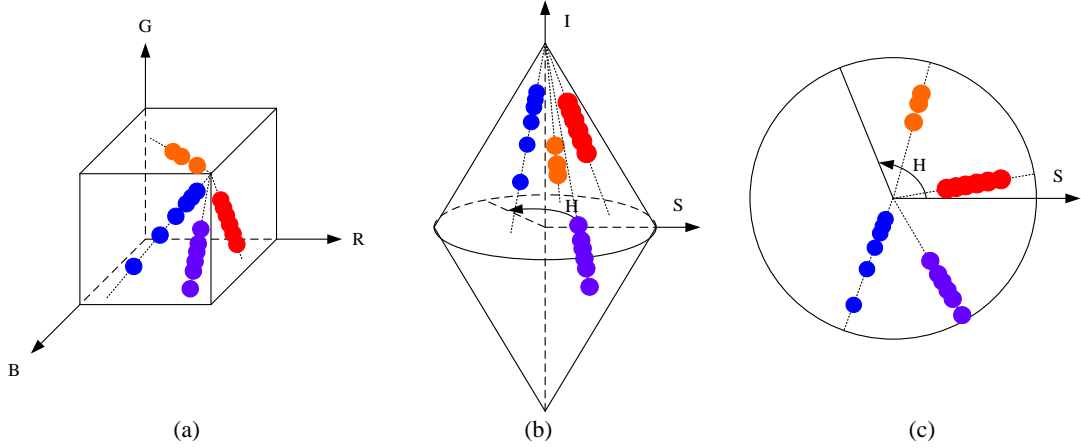


Fig. 7. Different forms of haze-lines; (a) Haze-lines in RGB space; (b) Haze-lines in HSI space; (c) Haze-lines are projected on to the HS plane.

(B) Transmission Map of I Channel

In essence, the I channel image is a gray image, satisfying the atmospheric scattering model which is shown in Eq. (1), and the I value has linear relationship with R, G and B values. Hence, Eq. (10) can be easily deduced.

$$I_j(i, j) = I_l(i, j)t(i, j) + I_A(1 - t(i, j)) \tag{10}$$

where  $I_j$  is the intensity of the hazy image,  $I_l$  is the intensity of the haze-free image, and  $I_A$  is the intensity of the atmospheric light.

Inspired by the infrared image defogging technology, some measures have been taken to calculate the transmission map of the single channel image. Li [31] observes single channel images and finds that gray value changes in regions with different relative depth information and the relative depth information of adjacent pixels is similar. Based on the observation, we take the I channel image as the depth map and deduce the transmission map.

$$t_0(i, j) = \alpha \left( \left(1 - \frac{1}{e}\right)(1 - I_l(i, j)) + \frac{1}{e} \right)^\beta \tag{11}$$

where  $\alpha$  is the compensation coefficient, and  $\beta$  is the atmospheric scattering coefficient. In our experiments, we find that when  $\alpha$  set to be 0.85 and  $\beta$  set to be 0.98 can provide the best performance.

(C) Transmission Map of S Channel

Since the process of calculating S values contain nonlinear operation, we cannot apply the atmospheric scattering model to variable S directly. For simplification, we make an assumption that the saturation of images still satisfies Eq. (1) and obtain Eq. (12).

$$S_j(i, j) = S_l(i, j)T(i, j) + S_A(1 - T(i, j)) \tag{12}$$

where  $S_I$  is the saturation of the hazy image,  $S_J$  is the saturation of the haze-free image,  $S_A$  is the saturation of the atmospheric light approximately equal to zero, and  $T$  is the transmission map of  $S$  channel which is different from  $t$  in Eq. (10). Therefore, Eq. (12) can be simplified to the following form:

$$S_J(i, j) = S_I(i, j)T(i, j). \quad (13)$$

Next, we can deduce the  $T$  based on the definition formula of saturation and Eq. (13).

$$T = \frac{I_I \cdot [I_J - \min(R_J, G_J, B_J)]}{I_J \cdot [I_I - \min(R_I, G_I, B_I)]} \quad (14)$$

Since the min operation will not change the relationship in Eq. (10), we can deduce the following equation:

$$\min(R_J, G_J, B_J) = t \cdot \min(R_I, G_I, B_I) + (1 - t) \cdot \min(R_A, G_A, B_A). \quad (15)$$

Besides, the airlight in haze conditions is nearly pure white. Thus, the  $R$ ,  $G$  and  $B$  values equal approximately that Eq. (16) can be deduced.

$$I_A \approx \min(R_A, G_A, B_A) \quad (16)$$

Now, we can get the simple Eq. (17) by inserting Eq. (10), (15) and (16) into Eq. (14).

$$T = \frac{I_I}{I_J} \cdot t \quad (17)$$

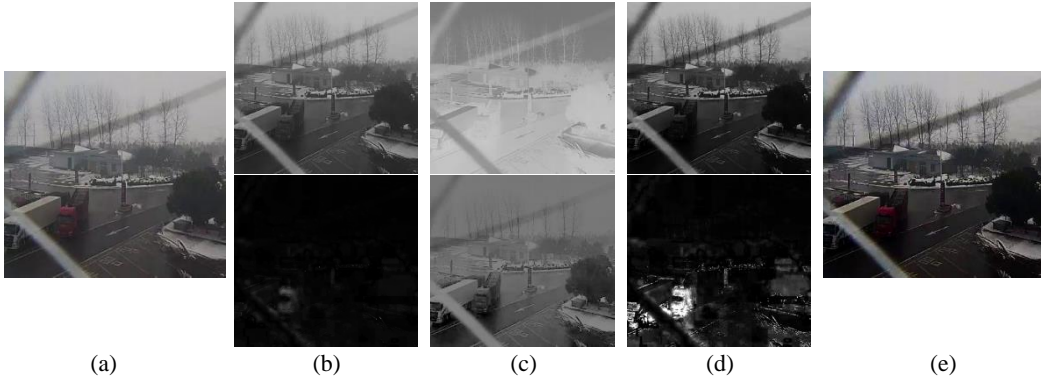


Fig. 8. Preliminary haze removal result; (a) Input hazy image; (b) I channel and S channel of hazy images; (c) Transmission maps of I channel and S channel; (d) Dehazing results of I channel and S channel; (e) Dehazing result of input hazy image.

### 3.4 Image Enhancement

Fig. 8 (d) shows the haze removal images in  $I$  and  $S$  channels, and we keep the hue values fixed and transform the dehazing result back to RGB color space. Fig. 8 (e) shows the final image. From the results, we can clearly see that our method can solve the problems of

color distortion and halo artifacts, but it still suffers from missing details for partial darkness.

Thus, image enhancement as a post-processing step is carried out to ensure a visual pleasing result. We try various approaches (*e.g.*, gamma correction, contrast limited adaptive histogram equalization (CLAHE), guided image filtering, *etc.*) to handle the problem of partial darkness and restore more detail information. Note that Gamma correction and CLAHE can handle the problem of partial darkness well, but gamma correction causes overexposure and CLAHE worsens the problem of missing details. Guided image filtering restores more detail information but worsens the problem of partial darkness. Therefore, we propose a novel post-processing method that includes the following three steps:

- Step 1:** Improve the overall image brightness by multiplying a constant parameter  $K$  which is determined by the image itself.
- Step 2:** Improve the local image brightness by CLAHE, set the contrast enhancement limit parameter to 0.001, and the desired histogram shape parameter to ‘rayleigh’.
- Step 3:** Highlight detail information by guided image filtering, set the local window radius parameter to be 15, and the regularization parameter to be 0.004.

Fig. 9 shows the intermediate results of post-processing. Compared with Fig. 9 (a), the visibility of Fig. 9 (d) improves apparently. Note that the constant parameter  $K$  is related with the pixel values of sky region. Hence, we can take advantage of the sky segmentation results to get the  $K$  value. First, the number of sky pixels  $N_{sky}$  is counted. Then, the intensity values of the hazy image are arranged from large to small. Next, the intensity value  $I_{sky}$  whose index is equal to  $N_{sky}$  are found. Finally, the constant parameter  $K$  approximately equal to the reciprocal of  $I_{sky}$ .



Fig. 9. Image enhancement result; (a) Preliminary dehazing result; (b) Overall brightness improvement result; (c) Local brightness improvement result; (d) Detail enhancement result.

#### 4. EXPERIMENTAL RESULTS

To demonstrate the effectiveness of the proposed algorithm, a large number of experiments have been done in different conditions including synthetic images and real-world images. Note that image enhancement is executed as post-processing of other dehazing methods for fairness. We compare the dehazing results with the state-of-the-art methods, such as dark channel prior (DCP) [14], Tarel [15], boundary constrained context regularization (BCCR) [16], non-local image dehazing (NLD) [17], color attenuation prior (CAP) [18], DehazeNet [23] and AOD-Net [24]. Note that the most of the following experiments

are implemented in MATLAB R2019b on an Intel Core i7 3.19Ghz PC with 16GB RAM; especially, AOD-Net is implemented in Pytorch on an Intel PC with GTX1660Ti GPU.

#### 4.1 Qualitative Comparison

##### (A) Synthetic Image Tests

In our experiments, the eight algorithms are tested using the synthetic hazy images from the SOTS dataset which contains 1000 synthetic test images [32]. One can clearly see that the DCP method can remove most of the haze. However, compared with the ground truth images, most regions of the images seem too dark especially in non-sky regions. Besides, the dehazing results of sky regions may be bad for invalid dark channel prior. For example, color deviation of the white clouds in the first image and third image, halo artifacts in the fourth image and fifth image, and some noise in the second image, *etc.* Tarel's method can remove most of the haze except the corners or gaps, such as the corners of the buildings and the gaps of the cars in the fourth image. Besides, his results suffer from over-enhancement. For example, the road in the fourth image is darker than it should be, and the color of the pedestrian's clothes in the fifth image is different from the ground truth. As can be seen in the figure, the results generated by the BCCR method share the similar visual effects with the DCP method. Although it overcomes the problem of partial darkness especially in non-sky regions, the problems of halo artifacts and noise are worse in sky regions. Compared with the above methods, the NLD method makes a good performance in non-sky regions from the first to the fourth image, but the haze around the pedestrians in the fifth image still exist. Besides, this method still cannot keep the fidelity of the sky regions in most images. From the results generated by the CAP method, we can find all dehazing images are natural and have no halo artifacts. Comparing with the ground truth, we find most regions of the CAP method is satisfying except the road regions which are darker than those in the ground truth. Compared with the conventional methods, the dehazing results of deep learning-based methods seem more natural and contain no halo artifacts. However, the color deviation phenomenon widely exists in the results generated by the AOD-Net method, especially in real-world images. Besides, the DehazeNet method can remove most haze in near regions, but the dehazing effect is poor in distant regions.

As can be seen in the next-to-last row of Fig. 10, the proposed method has no such problems. The haze of our method is totally removed, especially around corners and gaps. The sky regions are natural and have no halo artifacts, the non-sky regions are bright especially in road regions, and the details of the scene objects in our results are also rich.



Fig. 10. Dehazed results compared with state-of-the-art methods on synthetic hazy images.

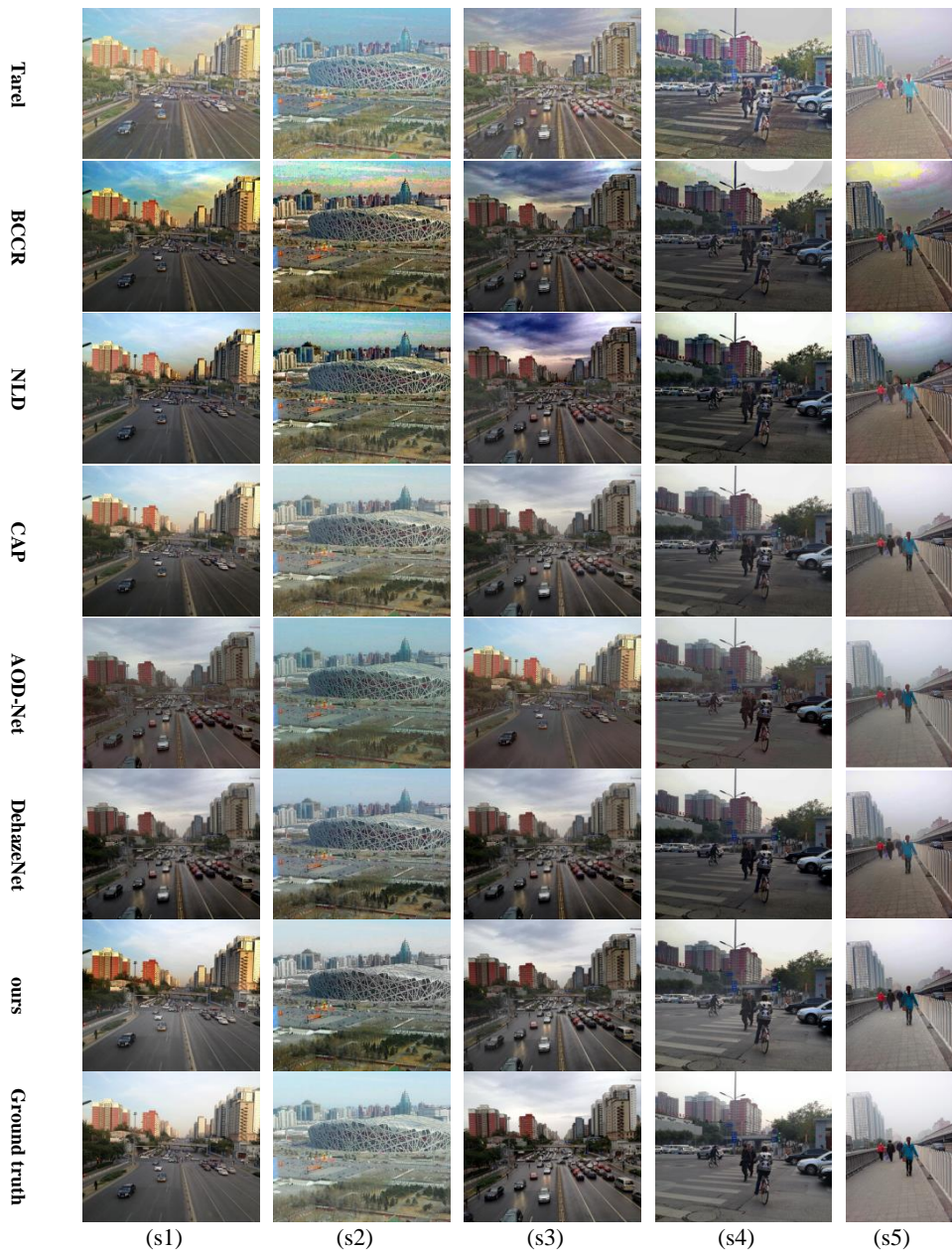


Fig. 10. (Cont'd) Dehazed results compared with state-of-the-art methods on synthetic hazy images.

(B) Real-World Image Tests

Apart from synthetic images, we also collect some challenging real-world images to compare with the above six algorithms. These images can be divided into two categories: general environment and dark environment.

In general environment, most conventional methods can remove most of the haze except the results of the CAP method contain white blocks in the third image and fourth image. But the CAP method can keep the fidelity of the sky regions which is the deficiency of other methods. In contrast, the deep learning-based methods contain few halo artifacts and the fidelity of sky regions is better than conventional methods. In general, the dehazing results of DehazeNet method have a comparable perception with our results. Besides, in our experiments we also find that the dehazing results of all the methods suffer from partial darkness, but the final results are pleasing due to our effective post-processing. Thus, we can deduce that all the results generated by the existing state-of-the-art methods share similar defects with synthetic images, but even more serious is the contrast and color of the dehazing results. From experimental results we can see that the proposed method can totally remove the haze, keep the color natural and restore more details, as shown in Fig. 11.

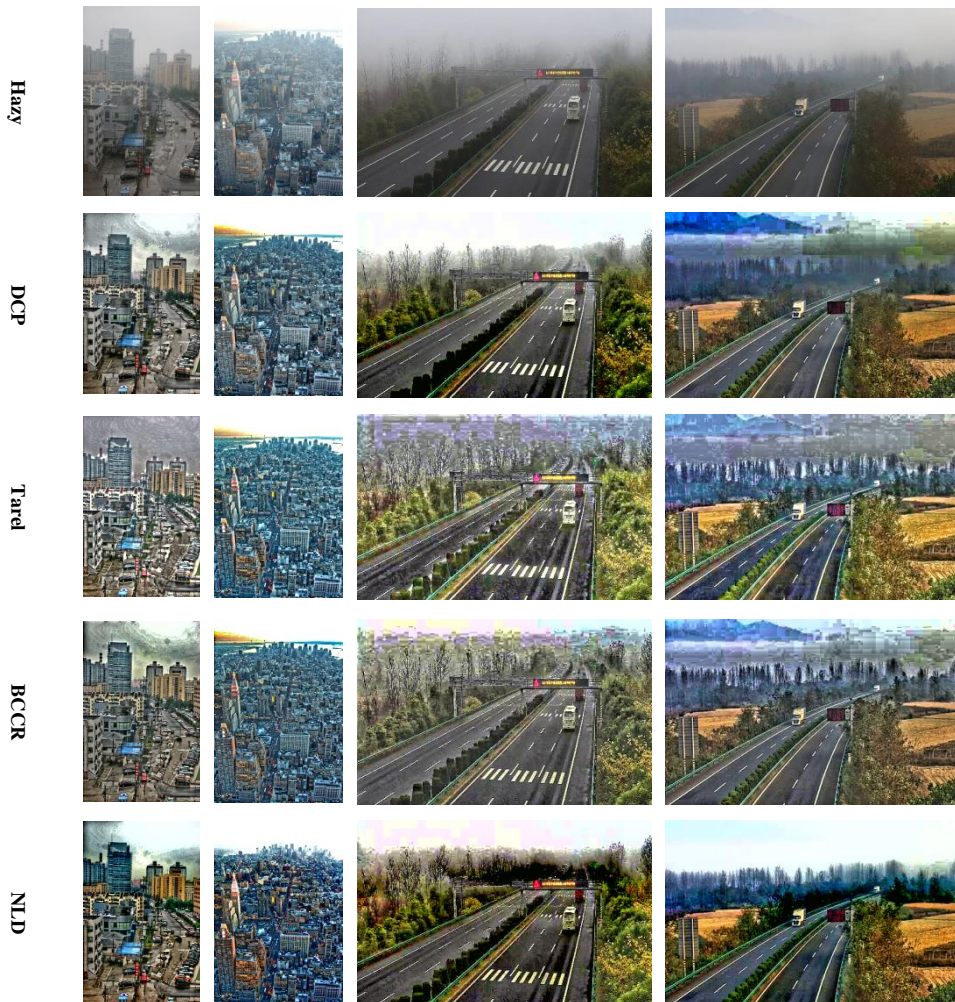


Fig. 11. Different dehazed results on the general environment of the real-world hazy images.

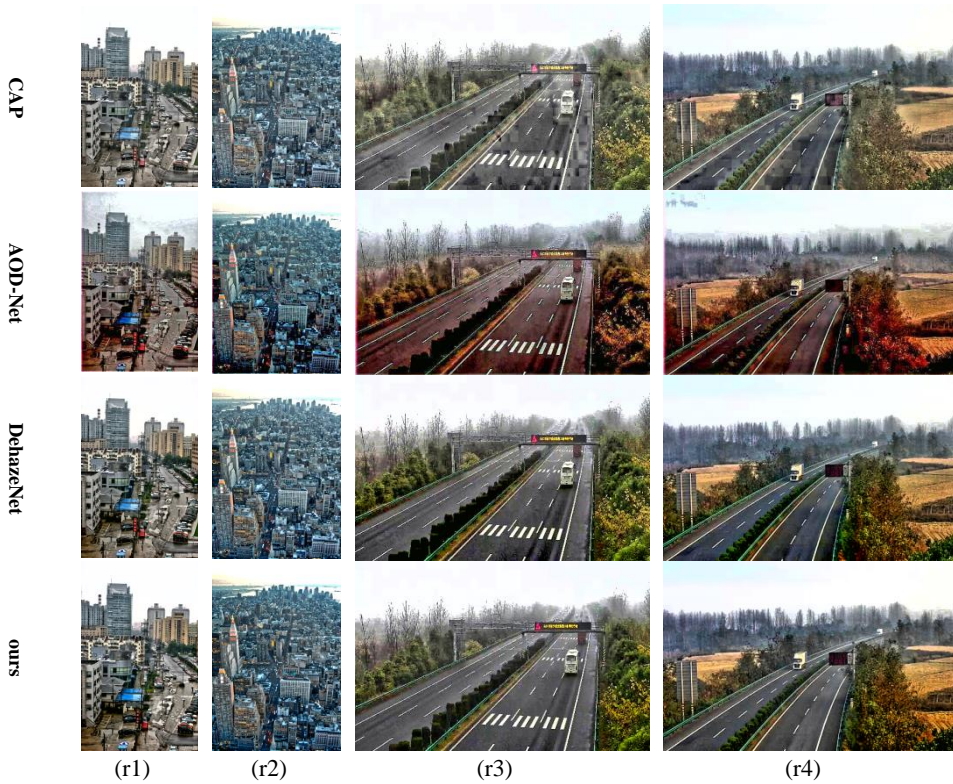


Fig. 11. (Cont'd) Different dehazed results on the general environment of the real-world hazy images.

For dark environment, the problems of color deviation and partial darkness are worse than that in general environment. As we can be seen in Fig. 12, the roads turn blue in the first image and second image obtained by DCP method, Tarel’s method, NLD method and DehazeNet method. The jungles in the first image and second image obtained by DCP method, AOD-Net method and DehazeNet method also seem too dark. In contrast, the proposed method can remove most haze, increase the brightness, keep the color fidelity, and restore more detail information as well, as shown in Fig. 12.



Fig. 12. Different dehazed results on the dark environment of the real-world hazy images.

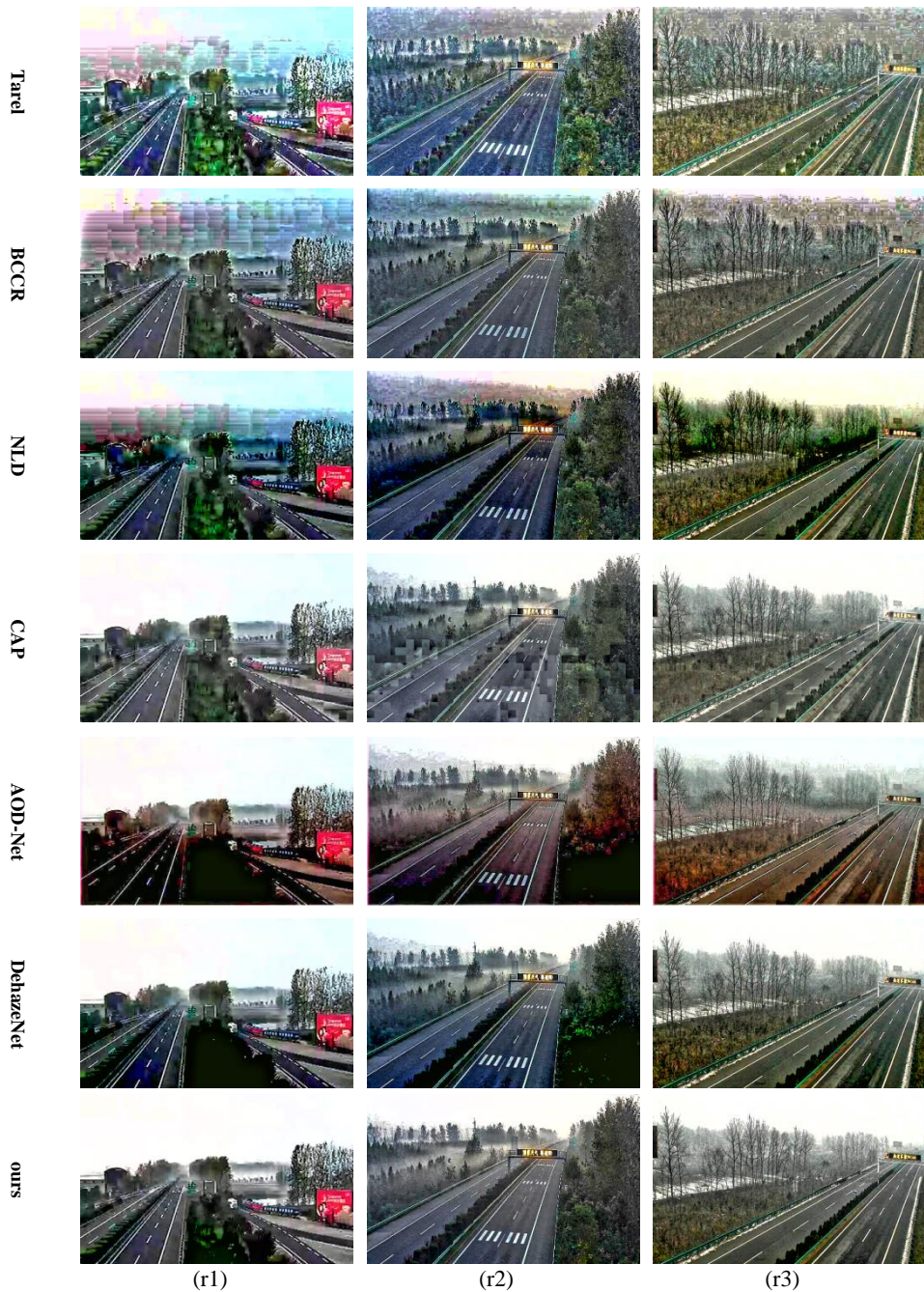


Fig. 12. (Cont'd) Different dehazed results on the dark environment of the real-world hazy images.

The simulation was built using a MATLAB simulator. The collisions are not discussed under the assumption that they can be solved using MAC layer protocols, and the

signals can be received only in LOS propagation. In simulation, we derived a transmit power value by a real distance in Eq. (4) and we can obtain a simulated distance by applied this transmit power value in Eq. (1). Each node was forced to remain active during the localization. The sensor nodes were deployed in an effective  $300 \times 300\text{m}$  area that was free from obstacles, and 100 sensor nodes were randomly deployed as a Gaussian distribution. In addition, the degree of irregularity (DOI) in the radio propagation model was applied in the simulation to determine whether the proposed scheme would be practical [16].

## 4.2 Quantitative Comparison

### (A) Synthetic Image Tests

To quantitatively assess the performance of six algorithms in synthetic images, we calculate the MSE and SSIM [33] of the results in Fig. 10 for comparison. The MSE can be calculated as:

$$\text{MSE} = \frac{1}{N} \sum \|J^{gray} - G^{gray}\|^2 \quad (18)$$

where  $J^{gray}$  is the gray image of the dehazing image,  $G^{gray}$  is the gray image of the ground truth image, and  $N$  is the number of pixels within the image. A lower MSE represents a better dehazing effect. The index of SSIM is used to evaluate the ability to preserve the structural information of the algorithms. A higher SSIM means that the dehazing image shares more similarity with the ground truth image, so the result is more acceptable.

**Table 1. MSE and SSIM values on the synthetic images in Fig. 10.**

| Method    | MSE          |              |              |              |              |              | SSIM         |              |              |              |              |              |
|-----------|--------------|--------------|--------------|--------------|--------------|--------------|--------------|--------------|--------------|--------------|--------------|--------------|
|           | s1           | s2           | s3           | s4           | s5           | Mean         | s1           | s2           | s3           | s4           | s5           | Mean         |
| DCP       | 2450.5       | 1393.5       | 8042.2       | 2137.6       | 7337.2       | 4272.2       | 78.4%        | 85.7%        | 55.6%        | 80.0%        | 54.5%        | 70.8%        |
| Tarel     | 1604.3       | 888.7        | 2623.0       | 1326.0       | 1260.0       | 1540.4       | 81.7%        | 89.3%        | 76.4%        | 78.4%        | 87.6%        | 82.7%        |
| BCCR      | 1923.1       | 2739.2       | 3404.2       | 2143.5       | 5044.3       | 3050.9       | 83.6%        | 71.1%        | 81.1%        | 83.0%        | 72.0%        | 78.2%        |
| NLD       | 768.4        | 2404.9       | 2854.8       | 1727.5       | 3287.8       | 2208.7       | 92.0%        | 78.3%        | 81.2%        | 83.5%        | 80.1%        | 83.0%        |
| CAP       | <b>339.6</b> | <b>313.3</b> | 547.1        | 657.9        | 686.0        | 508.8        | 93.9%        | <b>97.4%</b> | 91.9%        | 93.2%        | 94.9%        | 94.3%        |
| AOD-Net   | 360.4        | 1251.9       | 850.5        | 741.3        | 507.1        | 742.2        | 92.5%        | 89.3%        | 87.1%        | 86.7%        | 92.3%        | 89.6%        |
| DehazeNet | 616.5        | 933.9        | 566.2        | 913.8        | 930.8        | 792.2        | 89.4%        | 95.7%        | 93.9%        | 89.7%        | 94.8%        | 92.7%        |
| ours      | 371.7        | 968.2        | <b>250.4</b> | <b>380.5</b> | <b>444.1</b> | <b>483.0</b> | <b>94.7%</b> | 92.4%        | <b>94.3%</b> | <b>95.1%</b> | <b>95.4%</b> | <b>94.4%</b> |

The quantitative results are shown in Table 1. The mean MSE of the DCP method is the highest and its mean SSIM is the lowest for its not-so-good performance in sky regions and partial darkness in non-sky regions. Since the BCCR method overcomes some shortcomings of the DCP method, it achieves better MSE and SSIM results. The performances of the NLD method and Tarel's method are medium and the dehazing results generated by the CAP method and our method are the best. For deep learning-based methods, their evaluation indexes are generally better than most conventional methods. Our results generally achieve the lowest MSE value and the highest SSIM value, which demonstrated that the proposed method outperforms the seven existing algorithms.

### (B) Real-World Image Tests

For objectively assessing the performance of six algorithms in real-world images, we

use two indexes – the mean gradient change rate  $r$  and the coefficient of black pixels  $\sigma$  [34] as the assessment indexes for detail restoration. Besides, two novel indexes are also adopted as the assessment of color fidelity [33, 34]. The calculation equations of the above indexes are shown in Eqs. (19)-(22).

$$r = r_j / r_l \quad (19)$$

where  $r_j$  is the mean gradient of the dehazing image, and  $r_l$  is the mean gradient of the hazy image. A higher  $r$  means that the dehazing image restores more details comparing with the hazy image.

$$\sigma = N_{J_{gray0}} / N \quad (20)$$

where  $N_{J_{gray0}}$  is the number of black pixels in the gray image of the dehazing image, and  $N$  is the number of pixels within the image. A lower  $\sigma$  means that the dehazing image can solve the partial darkness problem better.

$$HMSE = \frac{1}{N} \sum \|J^H - I^H\|^2 \quad (21)$$

where  $J^H$  is the hue image of the dehazing image,  $I^H$  is the hue image of the original image, and  $N$  is the number of pixels within the image.

$$\eta = \frac{N_{diff}}{N} \quad N_{diff} = \text{num}(\text{diff}(J^H - I^H) \leq 0.01) \quad (21)$$

where  $N_{diff}$  is the number of little change pixels between the dehazing hue image and original hue image, and  $N$  is the number of pixels within the image. A lower HMSE or  $\eta$  means that the dehazing image can solve the color deviation problem better.

Considering most conventional methods contain halo artifacts in sky regions, we just calculate the mean gradient change rate  $r$  in non-sky regions. The corresponding results are shown from Tables 2-5. It is obvious that the proposed method overcome the partial darkness problem and restore more detail information compared with other state-of-the-art methods. Besides, our post-processing method also helps other methods to overcome the above two problems. Therefore, we can deduce that our algorithm generally achieves the best results on all indexes, which is consistent with our subjective observations.

**Table 2. Mean gradient change rate on real-world images in Figs. 11 and 12.**

| Method    | $r$          |              |              |              |              |              |              |              |
|-----------|--------------|--------------|--------------|--------------|--------------|--------------|--------------|--------------|
|           | Fig. 11(r1)  | Fig. 11(r2)  | Fig. 11(r3)  | Fig. 11(r4)  | Fig. 12(r1)  | Fig. 12(r2)  | Fig. 12(r3)  | Mean         |
| DCP       | 2.886        | 2.088        | 2.857        | 4.140        | 2.674        | 3.759        | 4.764        | 3.310        |
| Tarel     | <b>3.682</b> | <b>2.872</b> | <b>4.438</b> | <b>5.016</b> | <b>4.063</b> | <b>5.151</b> | <b>5.904</b> | <b>4.447</b> |
| BCCR      | 3.089        | 2.133        | <b>3.491</b> | 4.206        | <b>3.219</b> | <b>4.110</b> | <b>5.027</b> | <b>3.611</b> |
| NLD       | <b>3.185</b> | <b>2.216</b> | 3.101        | 4.135        | 2.904        | <b>4.089</b> | <b>5.144</b> | 3.539        |
| CAP       | 2.369        | 1.873        | 3.094        | 4.068        | 2.580        | 3.271        | 3.706        | 2.994        |
| AOD-Net   | 2.596        | 2.137        | 2.975        | 4.086        | 2.661        | 3.622        | 4.294        | 3.196        |
| DehazeNet | 3.099        | 2.087        | 3.178        | <b>4.344</b> | 3.042        | 3.792        | 4.464        | 3.429        |
| ours      | <b>3.131</b> | <b>2.170</b> | <b>3.361</b> | <b>4.452</b> | <b>3.501</b> | 3.829        | 4.765        | <b>3.601</b> |

**Table 3. Coefficient of black pixels on real-world images in Figs. 11 and 12.**

| Method    | $\sigma$      |               |               |               |               |               |               | Mean          |
|-----------|---------------|---------------|---------------|---------------|---------------|---------------|---------------|---------------|
|           | Fig.11(r1)    | Fig.11(r2)    | Fig.11(r3)    | Fig.11(r4)    | Fig.12(r1)    | Fig.12(r2)    | Fig.12(r3)    |               |
| DCP       | <b>0.000%</b> | <b>0.000%</b> | 0.603%        | <b>0.000%</b> | 1.431%        | 1.830%        | 3.705%        | 1.081%        |
| Tarel     | <b>0.000%</b> |
| BCCR      | 0.052%        | <b>0.000%</b> | <b>0.000%</b> | <b>0.000%</b> | 0.009%        | <b>0.000%</b> | <b>0.000%</b> | 0.009%        |
| NLD       | 0.174%        | 0.718%        | 0.841%        | 1.305%        | <b>0.000%</b> | 0.058%        | 0.223%        | 0.474%        |
| CAP       | <b>0.000%</b> |
| AOD-Net   | 0.140%        | 0.131%        | 0.093%        | 0.053%        | 0.138%        | 0.174%        | 0.011%        | 0.106%        |
| DehazeNet | <b>0.000%</b> | <b>0.000%</b> | <b>0.000%</b> | <b>0.000%</b> | 0.624%        | 0.241%        | <b>0.000%</b> | 0.124%        |
| ours      | <b>0.000%</b> |

**Table 4. HMSE values on real-world images in Figs. 11 and 12.**

| Method    | HMSE        |             |              |              |              |              |              | Mean         |
|-----------|-------------|-------------|--------------|--------------|--------------|--------------|--------------|--------------|
|           | Fig.11(r1)  | Fig.11(r2)  | Fig.11(r3)   | Fig.11(r4)   | Fig.12(r1)   | Fig.12(r2)   | Fig.12(r3)   |              |
| DCP       | 1243.8      | 24.9        | 4846.0       | 1006.8       | 7401.2       | 3552.6       | 265.9        | 2620.2       |
| Tarel     | 1535.8      | <b>18.8</b> | 3413.1       | 2034.8       | 6943.5       | 5016.9       | 615.9        | 2797.0       |
| BCCR      | 2210.1      | 23.9        | 5239.1       | 1880.6       | 6693.5       | 3554.0       | 1969.3       | 3081.5       |
| NLD       | 1853.5      | 1859.1      | 6746.3       | 2085.8       | 7369.0       | 3628.2       | 320.0        | 3408.8       |
| CAP       | 1120.2      | 28.7        | 2763.7       | 1493.7       | 6415.9       | 2641.9       | <b>144.1</b> | 2086.9       |
| AOD-Net   | 5512.3      | 1742.9      | 5553.1       | 5248.6       | 9587.1       | 5949.9       | 2173.3       | 5109.6       |
| DehazeNet | 960.9       | 19.5        | 1074.2       | 1995.9       | 4454.9       | 2848.1       | 171.5        | 1646.4       |
| ours      | <b>60.6</b> | 192.0       | <b>210.1</b> | <b>322.3</b> | <b>883.8</b> | <b>928.4</b> | 172.1        | <b>395.6</b> |

**Table 5. Coefficient of color deviation pixels on real-world images.**

| Method    | $\eta$       |             |              |              |              |              |              | Mean         |
|-----------|--------------|-------------|--------------|--------------|--------------|--------------|--------------|--------------|
|           | Fig.11(r1)   | Fig.11(r2)  | Fig.11(r3)   | Fig.11(r4)   | Fig.12(r1)   | Fig.12(r2)   | Fig.12(r3)   |              |
| DCP       | 59.5%        | <b>7.1%</b> | 73.0%        | 49.4%        | 89.6%        | 95.0%        | 85.4%        | 65.6%        |
| Tarel     | 57.5%        | 24.9%       | 76.7%        | 74.8%        | 93.9%        | 92.4%        | 81.3%        | 71.6%        |
| BCCR      | 69.9%        | 7.2%        | 65.6%        | 43.0%        | 74.5%        | 78.9%        | 70.4%        | 58.5%        |
| NLD       | 72.3%        | 68.0%       | 79.8%        | 75.4%        | 92.5%        | 74.0%        | 84.5%        | 78.1%        |
| CAP       | 52.3%        | 7.9%        | 50.6%        | 53.7%        | 67.1%        | 76.6%        | 58.6%        | 52.4%        |
| AOD-Net   | 92.8%        | 70.3%       | 96.3%        | 94.8%        | 95.6%        | 95.6%        | 96.7%        | 91.7%        |
| DehazeNet | 39.4%        | 9.4%        | 60.8%        | 63.3%        | 90.1%        | 95.0%        | 69.2%        | 61.0%        |
| ours      | <b>11.8%</b> | 12.7%       | <b>25.1%</b> | <b>28.1%</b> | <b>46.5%</b> | <b>32.1%</b> | <b>46.1%</b> | <b>28.9%</b> |

### (C) Complexity

In terms of time complexity, for an image of size  $r \times c$ , the complexity of the dehazing part is  $O(r \times c)$ . To reduce the executing time of sky segmentation and haze density division, we resize the input image to  $256 \times 256$ , which affect little final accuracy but save much time. Thus, the running time of our algorithm can be reduced to less than 1s. As shown in Table 6, the time consumption of our method increases slowly with the resolution increasing. It seems that the execution time of AOD-Net method has no relevance to image resolution for adequate computing power of GPU. The CAP method and our method are much faster than others, and our method makes a better performance on HD resolution. With the development of communication technologies, HD videos become common things in our daily life, thus our dehazing algorithm has a broader application prospect.

**Table 6. Time consumption comparison with the state-of-the-art dehazing methods.**

| Image Resolution | DCP      | Tarel   | BCCR    | NLD     | CAP           | AOD-Net | DehazeNet | ours          |
|------------------|----------|---------|---------|---------|---------------|---------|-----------|---------------|
| 640×345          | 11.930s  | 1.431s  | 1.683s  | 5.390s  | <b>0.453s</b> | 3.815s  | 1.427s    | 0.547s        |
| 400×600          | 12.428s  | 1.485s  | 1.711s  | 5.879s  | <b>0.496s</b> | 3.836s  | 1.537s    | 0.607s        |
| 576×768          | 23.056s  | 2.229s  | 2.325s  | 5.906s  | <b>0.712s</b> | 3.900s  | 3.041s    | 0.735s        |
| 1210×628         | 41.416s  | 6.064s  | 3.537s  | 8.002s  | 1.216s        | 3.886s  | 5.248s    | <b>1.094s</b> |
| 2074×1556        | 392.530s | 49.787s | 11.563s | 18.964s | 4.844s        | 4.058s  | 22.304s   | <b>3.428s</b> |

### 4.3 Traffic Scene Applications

In this section, two traffic applications, road marking features extraction and vehicle detection, are presented to verify the effectiveness of the proposed method.

#### (A) Road-Marking Features Extraction

Road-marking detection is an essential part in traffic scene, which can help the traffic police judge the legal liability in traffic accidents. Here, we utilize the gray histogram-based method to extract the road marking features. As can be seen in Fig. 13, the extraction results of DCP, BCCR and NLD methods make a little improvement compared with the original image. The CAP method extracts the least road-marking features, and the Tarel's method extracts the most of the road-marking features. However, compared with the result using our method, there are more non-marking pixels that are mistaken as the road marking features by using Tarel's method. That's because Tarel's method has over-enhancement problem. Thus, the conclusion that our method makes the best performance for more effective information extraction and less noise can be drawn.

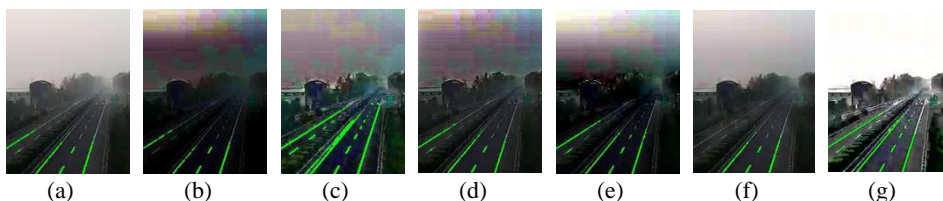


Fig. 13. Road-marking feature extraction results; (a) Feature extraction result for original image; (b) Feature extraction result for DCP method; (c) Feature extraction result for Tarel's method; (d) Feature extraction result for BCCR method; (e) Feature extraction result for NLD method; (f) Feature extraction result for CAP method; (g) Feature extraction result for our method.

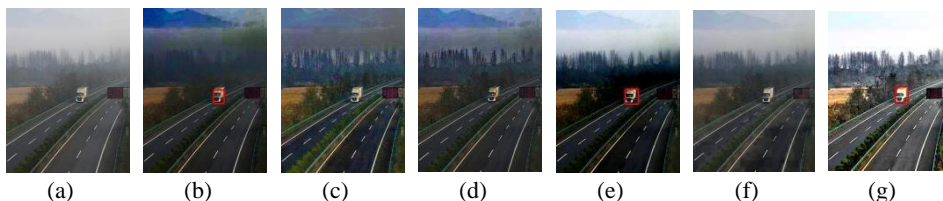


Fig. 14. Vehicle detection results; (a) Original image; (b) Detection result obtained by DCP method; (c) Detection result obtained by Tarel's method; (d) Detection result obtained by BCCR method; (e) Detection result obtained by NLD method; (f) Detection result obtained by CAP method; (g) Detection result obtained by our method.

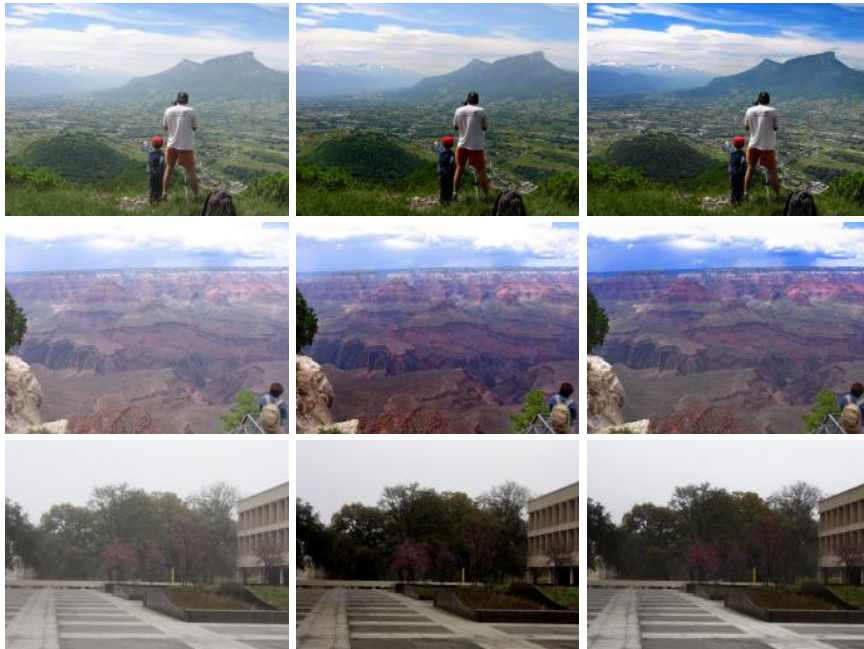
### (B) Vehicle Detection

The proposed dehazing method can also improve the detection of vehicles. We choose two thousand haze-free traffic images and collect the positive samples and negative samples. Then, the corresponding histogram of oriented gradient (HOG) features are calculated to train the SVM classifier. As shown in Fig. 14, we extract the HOG features of the seven images and perform vehicle detection. However, the white truck can't be detected in the original image and the images restored by Tarel, BCCR and CAP methods.

The red bounding boxes in the second, fifth and seventh images show that vehicle detection result in our restored image is most similar to the ground truth, when compared with the results in DCP and NLD restored images. Thus, many traffic scene applications can be benefit from the proposed algorithm.

## 5. DISCUSSION

To verify the generalization ability of our algorithm, a large quantity of experiments is carried out on other scenes. Some illustrative examples are shown in Fig. 15. Since the dehazing performance of DehazeNet method is better than other state-of-the-art methods in most cases, we thus choose it as a comparison target. As can be seen in Fig. 15, our algorithm can remove most haze in near regions and distant regions, while the DehazeNet method makes a poor performance in distant regions (*e.g.*, the mountain in the first image, and the horizon in the second image). Besides, the problem of partial darkness does not exist in our dehazing results, so more effective information can be extracted from the restored image (*e.g.*, jungles in the third image). Thus, we can deduce that although our algorithm is designed for traffic scene, it can perform well for other scenes as well.



(a) Original image. (b) DehazeNet method. (c) Our method.

Fig. 15. Dehazed results on other scene images.

## 5. CONCLUSIONS

Traditional haze removal methods suffer from the problems of color distortion, partial darkness and missing details. These problems will make a not-so-good performance in general and dark environment. To solve this problem, we propose an efficient traffic image dehazing method using sky segmentation and color space conversion. Specifically, in sky segmentation process, we propose two effective features including dark channel++ and contrast energy++ to separate the sky region in traffic scene. Since the atmospheric light is not always uniform in an image, we estimate the local atmospheric light based on the haze density. Then, the hazy image is transformed from the RGB color space to the HSI color space, and the restored I and S channel can be finally obtained. We also improve the local brightness and detail information by CLAHE and guided filtering, respectively. Besides, two traffic scene applications are introduced to verify the practicality of our method. The comparative experiments and quantitative evaluations showed that the proposed method could provide better results for traffic scene images compared with other representative algorithms. Besides, compared with deep learning-based methods, the proposed method also has competitive performance in the case of limited computing power or small-scale dataset.

## REFERENCES

1. E. J. McCartney, *Optics of the Atmosphere: Scattering by Molecules and Particles*, John Wiley and Sons, NY, 1976.
2. A. G. Khodary and H. A. Aly, "A new image-sequence haze removal system based on DM6446 davinci processor," in *Proceedings of IEEE Global Conference on Signal and Information Processing*, 2014, pp. 703-706.
3. X. Ji, J. Cheng, J. Bai, T. Zhang, and M. Wang, "Real-time enhancement of the image clarity for traffic video monitoring systems in haze," in *Proceedings of the International Congress on Image and Signal Processing*, 2014, pp. 11-15.
4. S. K. Nayar and S. G. Narasimhan, "Vision in bad weather," in *Proceedings of IEEE International Conference on Computer Vision*, 1999, pp. 820-827.
5. S. G. Narasimhan and S. K. Nayar, "Contrast restoration of weather degraded images," *IEEE Transactions on Pattern Analysis and Machine Intelligence*, Vol. 25, 2003, pp. 713-724.
6. S. G. Narasimhan and S. K. Nayar, "Vision and the atmosphere," *International Journal of Computer Vision*, Vol. 48, 2002, pp. 233-254.
7. S. G. Narasimhan and S. K. Nayar, "Removing weather effects from monochrome images," in *Proceedings of IEEE Computer Society Conference on Computer Vision and Pattern Recognition*, 2001, pp. 186-193.
8. Y. Y. Schechner, S. G. Narasimhan, and S. K. Nayar, "Instant dehazing of images using polarization," in *Proceedings of IEEE Computer Society Conference on Computer Vision and Pattern Recognition*, 2001, pp. 325-332.
9. H. Park, J. Park, H. Kim, and J. Paik, "Improved DCP-based image defogging using stereo images," in *Proceedings of IEEE International Conference on Consumer Electronics*, 2016, pp. 48-49.

10. G. Chen, T. Wang, and H. Zhou, "A novel physics-based method for restoration of foggy day images," *Journal of Image and Graphics*, Vol. 13, 2008, pp. 888-893.
11. S. G. Narasimhan and S. K. Nayar, "Removing weather effects from monochrome images," in *Proceedings of the IEEE Computer Society Conference on Computer Vision and Pattern Recognition*, 2001, pp. 186-193.
12. R. Tan, "Visibility in bad weather from a single image," in *Proceedings of IEEE Conference on Computer Vision and Pattern Recognition*, 2008, pp. 2347-2354.
13. R. Fattal, "Single image dehazing," *ACM Transactions on Graphics*, Vol. 27, 2008, pp. 72-80.
14. K. He, J. Sun, and X. Tang, "Single image haze removal using dark channel prior," *IEEE Transactions on Pattern Analysis and Machine Intelligence*, Vol. 33, 2011, pp. 2341-2353.
15. J. P. Tarel and N. Hautiere, "Fast visibility restoration from a single color or gray level image," in *Proceedings of IEEE International Conference on Computer Vision*, 2009, pp. 2201-2208.
16. G. Meng, Y. Wang, J. Duan, S. Xiang, and C. Pan, "Efficient image dehazing with boundary constraint and contextual regularization," in *Proceedings of IEEE International Conference on Computer Vision*, 2013, pp. 617-624.
17. D. Berman, T. Treibitz, and S. Avidan, "Non-local image dehazing," in *Proceedings of IEEE Conference on Computer Vision and Pattern Recognition*, 2016, pp. 1674-1682.
18. Q. Zhu, J. Mai, and L. Shao, "A fast single image haze removal algorithm using color attenuation prior," *IEEE Transactions on Image Processing*, Vol. 24, 2015, pp. 3522-3533.
19. X. Dong, X. Hu, S. Peng, and D. Wang, "Single color image dehazing using sparse priors," in *Proceedings of IEEE Conference on Image Processing*, 2010, pp. 26-29.
20. B. Li, S. Wang, J. Zheng, and L. Zheng, "Single image haze removal using content-adaptive dark channel and post enhancement," *IET Computer Vision*, Vol. 8, 2014, pp. 131-140.
21. P. Wang, Q. Fan, Y. Zhang, F. Bao, and C. Zhang, "A novel dehazing method for color fidelity and contrast enhancement on mobile devices," *IEEE Transactions on Consumer Electronics*, Vol. 65, 2019, pp. 47-56.
22. C. Qu, D. Bi, P. Sui, A. Chao, and Y. Wang, "Robust dehaze algorithm for degraded image of CMOS image sensors," *Sensors*, Vol. 17, 2017, No. 2175.
23. B. Cai, X. Xu, K. Jia, C. Qing, and D. Tao, "DehazeNet: An end-to-end system for single image haze removal," *arXiv*, 2016, arXiv:1601.07661.
24. B. Li, X. Peng, Z. Wang, J. Xu, and D. Feng, "AOD-Net: All-in-one dehazing network," in *Proceedings of IEEE International Conference on Computer Vision*, 2017, pp. 4770-4778.
25. I. Yoon, S. Jeong, J. Jeong, D. Seo, and J. Paik, "Wavelength-adaptive dehazing using histogram merging-based classification for UAV images," *Sensors*, Vol. 15, 2015, pp. 6633-6651.
26. H. D. Bhoir, N. M. Dongre, and R. R. Gulwani, "Visibility enhancement for remote surveillance system," in *Proceedings of IEEE International Conference on Inventive Computation Technologies*, 2016, pp. 348-351.

27. G. Yan, M. Yu, S. Shi, and C. Feng, "The recognition of traffic speed limit sign in hazy weather," *Journal of Intelligent & Fuzzy Systems*, Vol. 33, 2017, pp. 873-883.
28. T. Dong, G. Zhao, J. Wu, Y. Ye, and Y. Shen, "Efficient traffic video dehazing using adaptive dark channel prior and spatial-temporal correlations," *Sensors*, Vol. 19, 2019, p. 1593.
29. L. K. Choi, J. You, and A. C. Bovik, "Referenceless prediction of perceptual fog density and perceptual image defogging," *IEEE Transactions on Image Processing*, Vol. 24, 2015, pp. 3888-3901.
30. Y. Song, H. Luo, J. Ma, B. Hui, and Z. Chang, "Sky detection in hazy image," *Sensors*, Vol. 18, 2018, No. 1060.
31. Y. Li, Y. Zhang, Q. Zhang, A. Geng, and J. Chen, "Infrared image contrast enhancement based on defogging model," *Chinese Journal of Lasers*, Vol. 42, 2015, pp. 298-306.
32. B. Li, W. Ren, D. Fu, D. Tao, D. Feng, W. Zeng, and Z. Wang, "RESIDE: A benchmark for single image dehazing," *arXiv*, 2017, arXiv:1712.04143.
33. Z. Wang, A. C. Bovik, H. R. Sheikh, and E. P. Simoncelli, "Image quality assessment: From error visibility to structural similarity," *IEEE Transactions on Image Processing*, Vol. 13, 2004, pp. 600-612.
34. N. Hautière, J. P. Tarel, D. Aubert, and É. Dumont, "Blind contrast restoration assessment by gradient ratioing at visible edges," *Image Anal Stereol*, Vol. 27, 2008, pp. 87-95.



**Fan Guo (郭璠)** received the B.S. degree in Computer Science and Technology and the M.S. and Ph.D. degrees in Computer Application Technology from Central South University (CSU), Changsha, China, in 2005, 2008, and 2012, respectively. She is currently an Associate Professor with the School of Automation, CSU. Her main research interests include image processing, computer vision, and pattern recognition.



**Jun-Feng Qiu (邱俊峰)** is currently pursuing the M.S. degree in the Intelligent Information Processing and Intelligent System Laboratory, School of Automation, Central South University, Changsha, China. His research interests include digital image processing, computer vision, machine learning and embedded system.



**Jin Tang (唐璘)** received the B.S. degree and the M.S. degree from Peking University, Beijing, China, in 1987 and 1990, respectively, and the Ph.D. degree in pattern recognition and intelligence system from Central South University (CSU), Hunan, China, in 2002. He is currently a Professor in the School of Automation, CSU, Changsha. His current research interests are focused on image processing, pattern recognition and computer vision.



**Wei-Qing Li (李伟清)** currently pursuing the M.S. degree in the Intelligent Information Processing and Systems Laboratory, School of Automation, Central South University, Changsha, China. His research interests include deep learning, machine learning, and digital image processing.